

Fast Resonance Frequency Modulation in Superconducting Stripline Resonator

Eran Segev, Baleegh Abdo, *Student Member, IEEE*, Oleg Shtempluck, and Eyal Buks

Abstract—Fast resonance frequency modulation of a superconducting stripline resonator is investigated. The experiments are performed using a novel device which integrates a hot electron detector (HED) into a superconducting stripline ring resonator. Frequency modulation is demonstrated by both applying dc current or voltage to the HED, and by applying optical illumination, with modulation frequencies of up to 4.2GHz. Potential applications for such a device are in telecommunication, quantum cryptography and biofluorescence.

Index Terms—Parametric excitation, superconducting ring resonator, hot-electron detector, optoelectronics, NbN.

I. INTRODUCTION

RESONANCE parametric amplifiers are characterized by very low noise, high gain, and phase sensitive amplification. Parametric resonance in superconducting resonators [1] may allow some intriguing applications such as quantum squeezing [2], quantum non-demolition measurements [3], photon creation by the so-called dynamical Casimir effect [4], and more.

Parametric excitation occurs when the resonance frequency of an oscillator varies in time. The first parametric resonance occurs when the excitation is performed periodically at twice the resonance frequency f_0 , namely $f(t) = f_0 [1 + \xi \cos(4\pi f_0 t)]$ [5]. The system's response to such an excitation depends on the dimensionless parameter ξQ , where Q is the quality factor of the resonator. When $\xi Q < 1$ the system is said to be in the subthreshold regime, while above threshold, when $\xi Q > 1$, the system breaks into oscillation. Achieving parametric gain where $\xi Q > 1$ requires that the shift in the resonance frequency exceeds the width of its peak [6].

The frequency modulation mechanism, we employ here, is based on changing the boundary conditions of a superconducting resonator. This is done by switching a small section of the resonator to a normal state by using optical illumination. The switching time in superconductors is usually limited by the relaxation process of high-energy quasi-particles, also called 'hot-electrons', giving their energy to the lattice, and recombining to form Cooper pairs. Recent experiments with photodetectors, based on a thin layer of superconducting Niobium-Nitride (NbN), have demonstrated an intrinsic switching time on the order of 30ps and a counting rate exceeding 2GHz (see [7] and references therein). Resonance frequency shift

by optical radiation [8], [9], [10], or high-energy particles [11], [12] (for which the required condition $\xi Q \cong 1$ has been achieved) was demonstrated, though no periodic modulation was reported. Resonance frequency tuning [13] and switching [14] as well as optical and microwave signal mixing [15], [16] were demonstrated in normal-conducting GaAs microstrip ring resonators.

In this paper we show experimentally, that resonance frequency modulation, at twice the resonance frequency, is within reach using superconducting microwave resonators. Furthermore, the parametric gain threshold conditions, namely $\xi Q > 1$, is demonstrated in a continuous wave (CW) measurement. The experiments are performed using a novel device, that integrates a HED into a superconducting ring resonator. The HED is used as an optically tuned, lumped element, that changes the boundary conditions of the resonator [17], and thus manipulates its resonance frequencies.

In the following section we describe the circuit design and fabrication process. The results section starts with the HED response to applied dc voltage and current, and the resulting effect on the resonance frequencies. These results are followed by a comparison with a theoretical model. Afterwards, the effect of CW and modulated infrared (IR) light on the resonance frequency is described, and fast optical modulation of the resonance frequency is demonstrated.

II. CIRCUIT DESIGN AND FABRICATION

A. Circuit Design

The circuit layout is illustrated in Fig. 1(a). The device is made of 8nm thick NbN stripline, fabricated on a sapphire wafer, with dimensions of $34 \times 30 \times 1\text{mm}^3$. The design integrates three components. The first is a superconducting ring resonator and its feedline. Ring configuration is a symmetric and compact geometry, which is generally suitable for applications, which require resonance tuning [13]. The first few resonance frequencies are designed for the S&C bands (2 – 8GHz). The resonator is weakly coupled to its feedline, where the coupling gap is 0.4mm. The stripline width is set to $347\mu\text{m}$, to obtain a characteristic impedance of $Z_0 = 50\Omega$.

The second component is a HED, which is monolithically integrated into the ring structure. Its angular location, relative to the feedline coupling location, maximizes the RF current amplitude flowing through it, and thus maximizes its coupling to the resonator. The HED, shown in Fig. 1(b), has a $4 \times 4\mu\text{m}^2$ meander structure, consists of nine NbN superconducting strips. Each strip has a characteristic area of $0.15 \times 4\mu\text{m}^2$ and the strips are separated one from another by approximately $0.25\mu\text{m}$ [18].

This work was supported by MAFAT, Israel Science Foundation under grant 1380021, the Deborah Foundation and Poznanski Foundation.

The authors are with the Department of Electrical Engineering and Microelectronics Research Center, Technion, Haifa 32000, Israel (E-mail: segeve@tx.technion.ac.il).

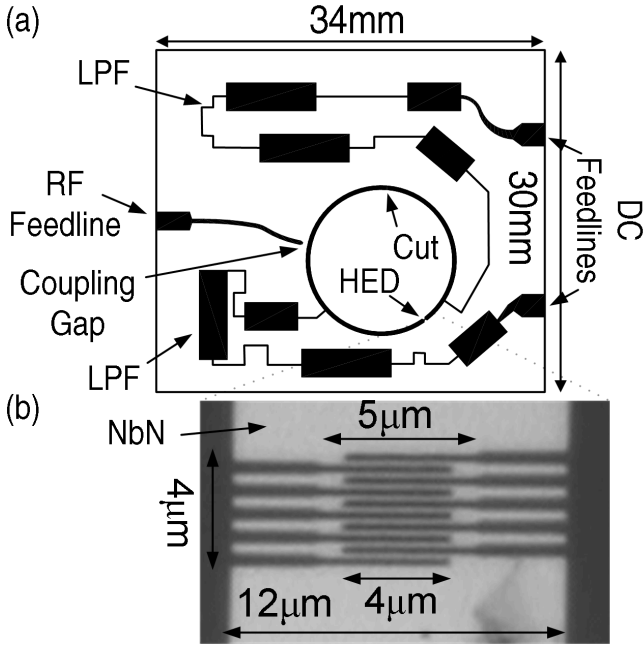


Fig. 1. (a) Device layout. (b) Optical microscope image of the HED.

The HED operating point is maintained by applying dc bias. The dc bias lines, forming the third component, are designed as two superconducting on-chip low-pass filters (LPF) with a cut-off frequency of 1.2GHz. As this frequency is lower than the fundamental resonance frequency of the resonator, the intrinsic fields of the resonator are not appreciably perturbed. A cut of $20\mu\text{m}$ is made in the perimeter of the resonator, to force the dc bias current flow through the HED.

The device, which is top covered by a bare sapphire substrate, is housed in a gold plated Faraday package made of Oxygen Free High Conductivity (OFHC) Copper. Superconducting Niobium ground planes are dc-magnetron sputtered on the inner covers of the package. RF power is fed using a SMA launcher, coupled to the feedline. A dc bias is fed through two π -LPFs, screwed to the package, having a cut-off frequency of 1MHz. IR laser light is guided to the device by a fiber optic cable. A through hole of 1mm in diameter, is drilled in the Faraday package, and a fiber optic connector affixes the tip of the fiber cable at approximately 9.55mm above the HED.

B. Fabrication Process

The fabrication process starts with a thorough pre-cleaning of the sapphire wafer in solvents. We have experienced that the commonly employed process of piranha followed by RCA cleaning substantially reduces the NbN adhesion to the Sapphire wafer. In the next step, 200nm thick gold pads are thermally evaporated through a mechanical mask to form the dc contact pads. The mask partially shadows the evaporation and thus the pads' perimeters are smoothed. Epitaxy, 8nm thick, NbN film is then deposited at 700°C using a dc-magnetron sputtering system [19]. Sputtering parameters are summarized in table I and the process itself is further detailed in [20]. Next, an AlN layer of 7nm thickness is *in-situ*

TABLE I
SPUTTERING PARAMETERS

Process parameter	NbN	AlN
Partial flow ratios (Ar,N ₂)	(87.5%,12.5%)	(0%,100%)
Base temperature	700 °C	60 °C
Base pressure	$3.6 \cdot 10^{-7}$ torr	$1.8 \cdot 10^{-7}$ torr
Work pressure	$6.8 \cdot 10^{-3}$ torr	$2.9 \cdot 10^{-3}$ torr
Discharge current	360mA	360mA
Discharge voltage	311V	292V
Deposition rate	$3.6\text{\AA}/\text{sec}$	$1.1\text{\AA}/\text{sec}$
Thickness (<i>t</i>)	8nm	7nm
Target-substrate distance	95mm	230mm

sputtered in N₂ atmosphere at a temperature smaller than 100°C . This layer protects the vulnerable NbN layer during the following fabrication processes and restrain degradation [21]. It has also a functional role, as at cryogenic temperatures, it serves as a thermal conducting layer, which enhances the cooling of the NbN layer. In the next step, the HED meander stripline is patterned using electron beam lithography (EBL). The deposition of a 80nm thick PMMA 950K layer is followed by EBL with the following parameters: 40kV, 15pA, and 2.1nC/cm, corresponding to acceleration voltage, emission current, and line dose respectively. Afterwards, the AlN layer is directly etched through the PMMA mask using ion milling. The remaining AlN layer serves as a mask for the sequential etching of the NbN layer, using low power reactive ion etching (RIE) in SF₆ environment [22]. The remaining PMMA is removed by NMP. The last fabrication step is the patterning of the resonator and the LPFs features. This is achieved by using standard photolithography process. The photoresist development process (employing AZ-326 photoresist developer), also wet etches the AlN layer, while the remaining layer is again used as a mask for the RIE etching of the NbN film.

III. EXPERIMENTAL AND NUMERICAL RESULTS

All measurements presented in this paper are carried out in a fully immersed sample in liquid helium (4.2K). The experimental setup, used for reflection measurements, is schematically depicted in Fig. 2. The samples's RF feedline is connected to a vector network analyzer using a semi-rigid coax cable. The dc feedlines are connected to a dc source-measure unit using 4-probe wiring. The laser source has a wavelength of 1550nm.

A. DC I-V Measurements

The basic I-V characteristics of the HED meander stripline, shown in Fig 3, exhibit a highly complex hysteretic behavior. Panel 3(a) plots nine current measurements, obtained while increasing the applied voltage (blue), one on top of the other, where each measurement starts at zero voltage and ends at a different maximum voltage, slightly above the voltages V_{Cn} , depicted in the figure. The corresponding nine current measurements, obtained while decreasing the applied

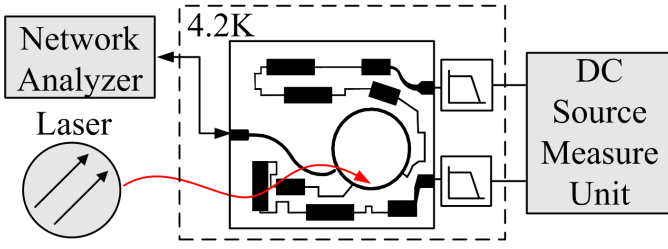


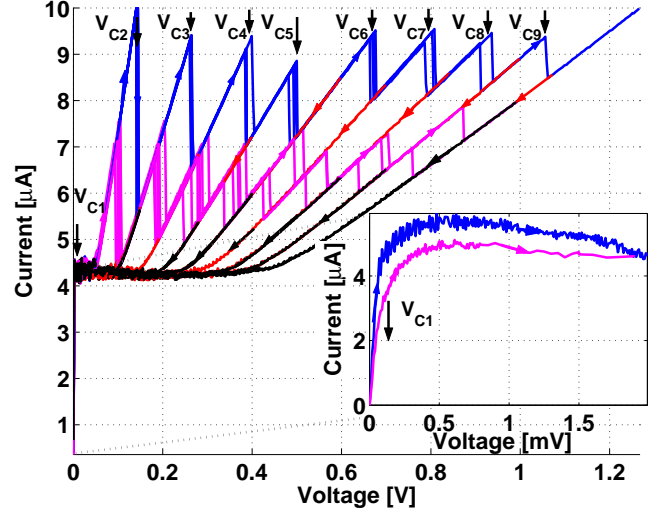
Fig. 2. Setup used for reflection measurements.

voltage are also plotted (red). The magenta and black curves correspond to similar measurements, taken while the HED is being illuminated. The measurements for low applied voltages and currents are enlarged in the insets of Fig 3(a) and (b) respectively, where the finite resistance is due to the contacts.

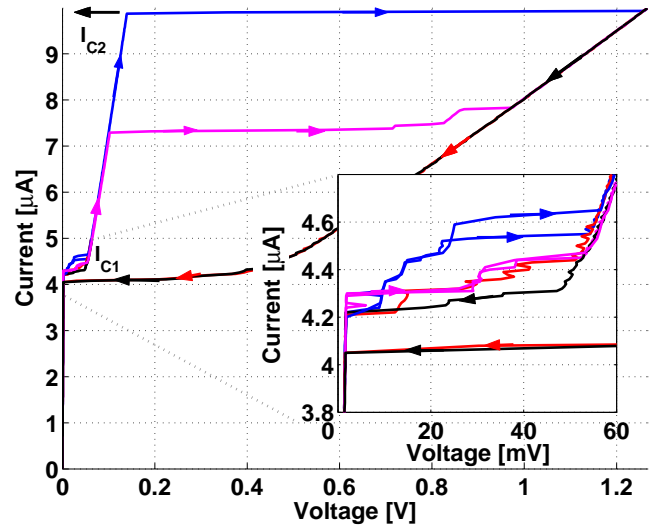
At panel 3(a), nine, clearly distinguished, abrupt jumps in the measured current are noticed. The number of current jumps corresponds to the number of stripline sections that compose the meander shape of the HED. Each jump is the result of a large increase in the HED resistance due to a transition of one section from the superconducting state to the normal one. This behavior is typical for a superconducting microbridge and is caused by the formation of a hotspot in the bridge area [23]. Each critical voltage V_{Cn} , varies, in general, between different scans, indicating thus, the stochastic nature of the transitions between bistable states. The fluctuation ΔV_{Cn} in V_{Cn} , between different scans, characterizes the lifetime of the pre-jump metastable states of the system. The increase in ΔV_{Cn} at high voltages indicates a decrease in the lifetime of metastable states because of larger temperature fluctuations. The combined results of the increasing and decreasing applied voltage measurements show that large hysteresis is present at all current jumps except for the first one. This observation indicates, that only one section at a time can be biased into subcritical conditions. Furthermore, only the section responsible for the first jump, at V_{C1} , doesn't suffer from hysteresis and thus can repetitively respond to radiation. Probably, the cause for this discretization of the critical current is the non-uniformity in the meander shape of the HED [23], [24]. Our finding clearly shows that the non-uniformity may substantially reduces the effective area of the HED, up to a fraction of 1/9 of its printed area.

The same measurements are repeated while constantly illuminating the HED with approximately 27nW IR laser. In these measurements the current jumps occur at lower applied voltages, $V'_{Cn} < V_{Cn}$. In addition, ΔV_{Cn} are substantially widened. Although the decrease in the critical voltage values can be explained by local heating due to the IR illumination, the increase in ΔV_{Cn} , especially at low voltages, imply that photon absorptions cause discrete events that considerably increase the instability of the HED.

Panel 3(b) shows voltage measurements, obtained while increasing the applied current, with (magenta) and without (blue) IR illumination, and while decreasing the applied current, with (black) and without (red) IR illumination. Two abrupt voltage jumps occur at distinguishable critical currents of $I_{C1} \cong$



(a)



(b)

Fig. 3. Basic I-V characteristic of the HED meander stripline. (a) Current vs. voltage and (b) voltage vs. current measurements. The magenta (blue) curves show an increasing applied voltage and current measurement, with (without) laser illumination. The black (red) curves show a decreasing applied voltage and current measurement, with (without) laser illumination. The insets of (a) and (b) magnify the results for small applied voltages and currents respectively.

$4.2\mu\text{A}$ and $I_{C2} \cong 9.8\mu\text{A}$. IR illumination has a negligible measured effect on I_{C1} and a strong effect on I_{C2} values. All voltage jumps suffer from hysteresis and therefore current bias is an unsuitable method for repetitive radiation detection.

B. DC I-V Effect on the Resonance Lineshape

Fig. 4 shows several $|S_{11}|$ measurements as a function of frequency, in the vicinity of the second resonance mode, for various HED resistance values. For clarity, the resonance curves are vertically shifted upwards, for increasing resistance values. The measurements are obtained while applying variable voltage V_b , and the resistance is measured simultaneously

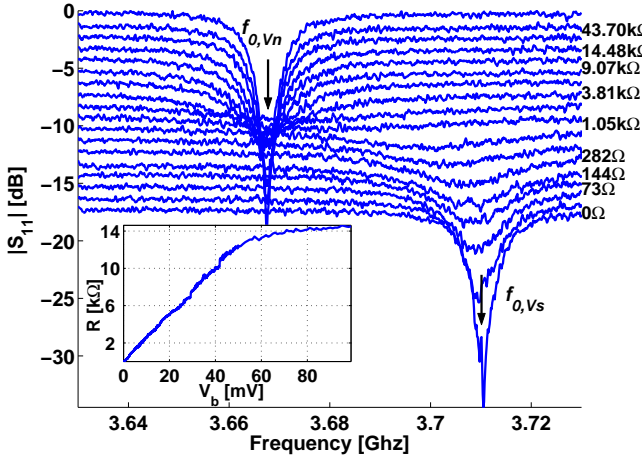


Fig. 4. Several $|S_{11}|$ measurements of the second resonance mode, as a function of frequency, for various HED resistance values. The measurements are obtained while applying variable voltage and the HED resistance is measured using 4-probe technique. Plots are shifted vertically for clarity. The inset shows the resistance vs. voltage characteristics of the HED.

with the $|S_{11}|$ data using standard 4-probe technique. The RF input power is set to -64.7 dBm, where the resonator is in the linear regime [25]. The inset of Fig. 4 plots the measured HED resistance as a function of V_b .

The dependence of the resonance characteristics on the HED resistance R_{HED} , can be described as followed. At zero applied voltage the resonance frequency is $f_{0,V_s} \cong 3.71$ GHz. At very low voltages, as the HED is biased far below critical conditions, its resistance is negligible and its influence on the resonance curve as well. As the resistance increases, the resonance frequency slightly red shifts, and more important, the Q -factor is significantly reduced due to dissipation in the HED. This behavior continues up to a point, at $R_{\text{HED}} \cong 1$ k Ω , where the resonance curve can be hardly detected. When increasing the resistance beyond that point the trend of the Q -factor changes, the dissipation decreases, and the resonance curve reemerges at a new resonance frequency, $f_{0,V_n} \cong 3.665$ GHz, red shifted by approximately 45 MHz relative to its original value. The new resonance Q -factor has a value similar to the original one. When further increasing the resistance, the trend of the Q -factor continues but no additional resonance shift occurs. The behavior of the Q -factor suggests that as R_{HED} increases, the RF current amplitude of the resonance mode in the HED is reduced, due to current redistribution, and thus the total power dissipation decreases.

Similar behavior, with one major exception, can be observed under applied current, as shown in Fig 5. The blue, green, red, and cyan curves are taken with subcritical $0 \mu\text{A}$, $4.33 \mu\text{A} < I_{C1}$, and over critical $4.39 \mu\text{A}$, $5 \mu\text{A} > I_{C1}$ applied currents, respectively, where I_{C1} is the current at which a first jump in the measured voltage occurs. There are two well defined resonance frequencies, $f_{0,I_s} = 3.83$ GHz, and $f_{0,I_n} = 3.79$ GHz, which corresponds to applied currents below, and above I_{C1} respectively. f_{0,I_s} , and f_{0,I_n} slightly differ from f_{0,V_s} , and f_{0,V_n} as the two measurements were taken at different thermal cooldown cycles. Low Q -factor curves are absent from this

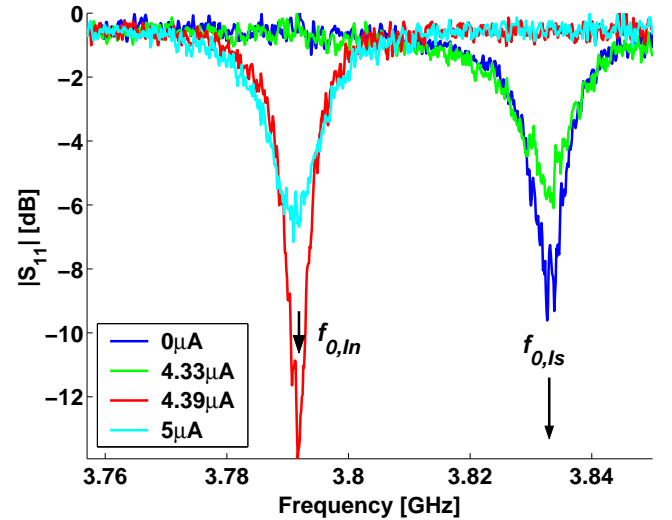


Fig. 5. Several $|S_{11}|$ measurements of the second resonance mode, as a function of frequency. The measurements are obtained while applying variable current.

measurement because under applied current, the HED can not be biased into intermediate resistance values. At bias currents below I_{C1} , the HED has low resistance, which only slightly increases as the current approaches I_{C1} . As a result, no resonance shift occurs, and only the Q -factor slightly reduces as the current increases. This behavior changes abruptly once the HED resistance crosses a rather low, critical value, R_C . A self-sustained hotspot is generated [23], quickly expands, and the HED becomes resistive. I_{C1} is the bias current at which $R_{\text{HED}} = R_C$ is obtained. This thermal runaway causes an abrupt red shift of $\Delta f_0 \cong 40$ MHz in the resonance frequency. Further increase of the bias current beyond I_{C1} increases the power dissipation and heat generation in the HED. This increases the local temperature and dissipation near the HED, and thus causes Q -factor reduction.

C. Resonance Frequency Shift Modeling

To account for our results we calculate the resonance characteristics of our device, as a function of HED resistance.

As shown in Fig. 6, the ring resonator is modeled as a straight transmission line, extending in the $\pm x$ directions. The HED is represented by a lumped discontinuity, $Z = R + j\omega L$, connecting $x = \pm b$ points together, where R is the resistance, ω is the angular frequency, and L is the total inductance of the meander shape of the HED. The transmission line has a cut at point $x = a$. The couplings to the RF and dc feedlines are neglected.

The voltage along the resonator's transmission line is given by a standing waves expression of the form [26]

$$V(x) = \begin{cases} A \cos(\beta x) + B \sin(\beta x) & -b < x < a \\ C \cos \beta(x - a) + D \sin \beta(x - a) & a < x < b \end{cases},$$

where $\beta = 2\pi f \sqrt{\epsilon_r}/c$ is the propagation constant along the transmission line, f is the frequency, ϵ_r is the relative dielectric constant, and c is the speed of light in vacuum.

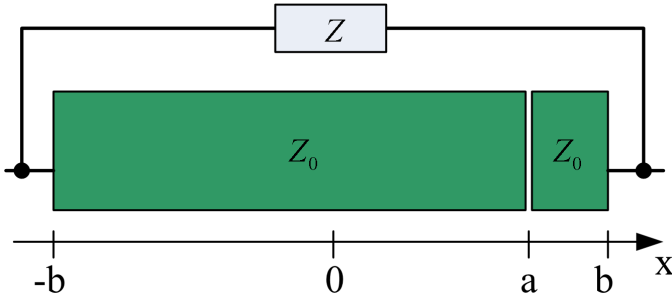


Fig. 6. Resonator model.

The current is given by $I(x) = (i/\beta Z_0) dV/dx$, where Z_0 is the characteristic impedance of the line. By applying the following boundary conditions: (1) $I(a_-) = I(a_+) = 0$, (2) $I(-b) = I(b)$, and (3) $V(b) - V(-b) = I(b)Z$, we easily derive a boundary condition equation which yields the complex resonance frequencies of the resonator.

A phase transition of Z from superconducting to normal state simultaneously causes changes in its resistive, $\Delta R > 0$, and inductive, $\Delta L > 0$, parts. Both changes contribute to a resonance shift in the same direction. For a very thin superconducting films $\Delta R \gg \Delta L$ resulting in $\Delta Z \cong \Delta R$. Three fitting parameters are used in the model. Best fit results are obtained for $R = 0\Omega$, $Z_0 = 55\Omega$, and $\omega L = 14.5Z_0$, which leads to $L = 37.3\text{nH}$ for the second resonance mode. $R \ll Z_0$ in the superconducting state, and thus negligible. The characteristic impedance Z_0 value is in a very good agreement with the designed value of 50Ω . The calculated inductance L of the meander line at 4.2K without any applied current is 6.05nH [27], but this value is strongly dependant on temperature and current density, so the fit parameter value is in reasonable agreement with the calculated one [27], [28].

Table II summarizes the first three solutions of the boundary condition equation for the two extreme cases of $\Delta R = 0$ and $\Delta R \rightarrow \infty$. Comparing these results to the measured results (taken at two different cooldown cycles), also summarized in table II, shows a good agreement, especially for the second and third modes, for which the resonator is designed.

Fig. 7 shows the second resonance characteristics, resonance frequency and unloaded damping rate γ_2 [2], of the experimental data (blue) and the numerically calculated data (red). The rate γ_2 is extracted from the data plotted in Fig. 4 using the method presented in the appendix. The upper subplot shows the resonance frequency as a function of ΔR . The calculated resonance frequency, at zero resistance, is $f_0 = 3.791\text{GHz}$, which equals the mean value of the resonance frequency measured at different cooldown cycles. In this subplot, the calculated data is corrected by -80MHz to overlap between the first calculated and measured point. Both curves show the same dependence on ΔR . The lower subplot shows the unloaded damping rate γ_2 , as a function of ΔR . Also in this case, a good agreement with the experiment is obtained, and as expected, the measured damping rate exceeds the calculated one, due to losses, which are not taken into account in the model.

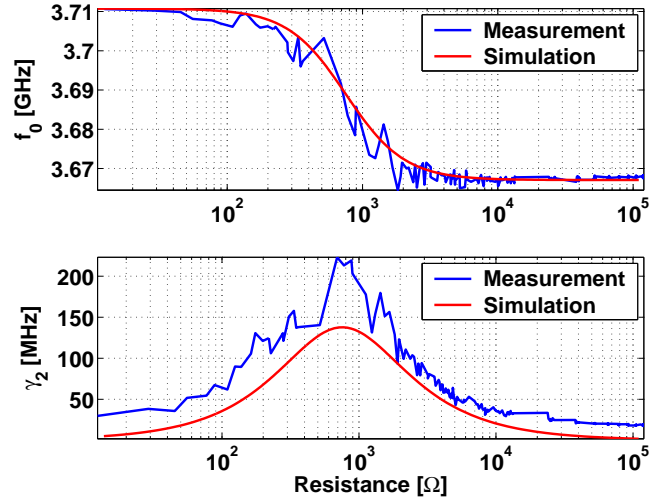


Fig. 7. Resonance frequency and unloaded damping rate γ_2 of the second resonance mode.

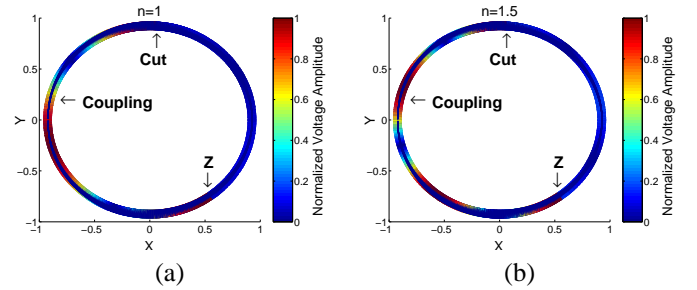


Fig. 8. Normalized voltage amplitudes as a function of the ring's angular location, for the (a) second and (b) third resonance modes.

The coupling between the different modes and the HED can be characterized by the current amplitude through the HED. The model predicts normalized current amplitudes of 7.3% and 5.7% inside the lumped element, for the second and third modes respectively. This rather weak coupling is the result of the rather high kinetic inductance of the HED. To estimate the coupling of modes two and three to the feedline [29], we show in Fig. 8 the normalized voltage amplitudes, as a function of the ring's angular location. The calculated normalized voltage amplitudes, at the feedline coupling location, are 71% and 92%, respectively. The voltage amplitudes distribution have, in general, a strong dependence on the resonance frequency, and hence on ΔR , but because of the rather small resonance shift, the voltage amplitudes at the coupling location change by less than 2%.

D. IR Illumination Effect on the Resonance Lineshape

Fig. 9 plots $|S_{11}|$ measurements with (red) and without (blue) IR illumination. The effective IR illumination power, impinging on the HED, is approximately 27nW . The RF input power is set to -64.7dBm and the HED is biased with a subcritical dc current of $4.14\mu\text{A}$, which only weakly influences the resonance curve. When the illumination is turned on, the resonance frequency abruptly shifts to a lower frequency.

TABLE II
RESONANCE FREQUENCY CHARACTERISTICS

n	Numerical Results			Experimental Results		
	f_0 [GHz] $\Delta R = 0$	f_0 [GHz] $\Delta R \rightarrow \infty$	Δf_0 [MHz]	f_0 [GHz] $\Delta R = 0$	f_0 [GHz] $\Delta R \rightarrow \infty$	Δf_0 [MHz]
1	1.913	1.873	39.8	1.59	1.58	10
2	3.791	3.747	43.7	3.874, 3.711	3.829, 3.668	45, 43
3	5.654	5.62	34.1	5.634, 5.38	5.608, 5.35	26, 30

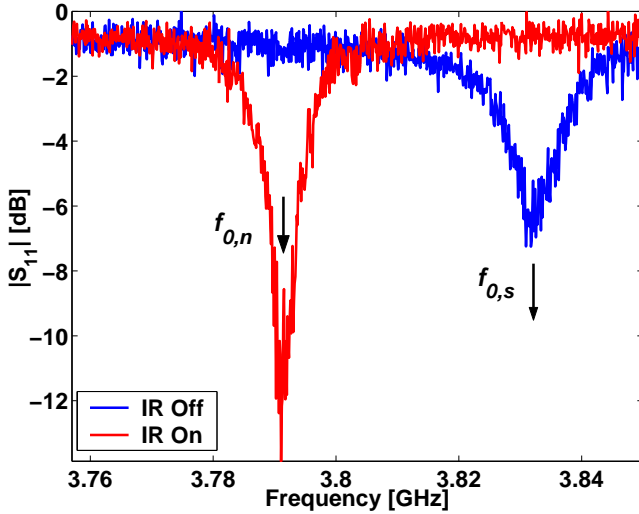


Fig. 9. Several $|S_{11}|$ measurements of the second resonance mode, as a function of frequency, while applying sub-critical current, with (red) and without (blue) IR illumination.

The new resonance lineshape has the same characteristics as the resonance lineshape measured without illumination under supercritical bias current of $I = 4.39\mu\text{A} > I_{C1}$. This measurement clearly shows that the resonance frequency is sensitive to IR illumination. The measured results in this experiment yield $\xi Q \cong 4.14$.

E. Fast Modulation of the Resonance Frequency

Fast modulation of the resonance frequency is performed using the experimental setup depicted in Fig. 10. The resonator is excited by a CW pump signal, at frequency $f_0 = 3.71\text{GHz}$, which coincides with the second resonance frequency. The optical signal is modulated at frequency Δf , using a Mach-Zener modulator driven by a second CW signal, phase locked with the first one. The reflected power is mainly composed of three tones. One is the reflected pump signal at frequency f_0 . The other two are sidebands, produced by mixing the pump signal and the optical modulation signal, and are found at frequencies $f_{1,2} = f_0 \pm \Delta f$. Occasionally, higher orders of the mixed signals are also detected. The amplified reflected power is measured using a spectrum analyzer, which tracks the $f_1 = f_0 + \Delta f$ tone. No dc bias is needed in this measurement as the RF probe signal also serves as a bias signal for the HED. This bias scheme has two major advantages over the dc bias

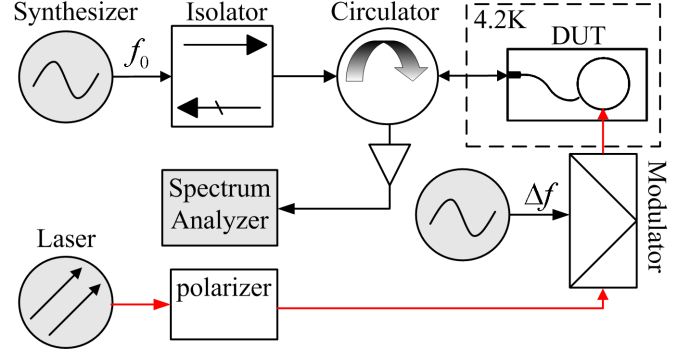


Fig. 10. Setup used for frequency modulation.

scheme; first the RF pump bias signal has lower noise, as the $1/f$ and line noises are avoided. Second, the RF bias signal introduces a strong non-linear mechanism [25], [30], which will be discussed in a future publication [31], and produces a high internal gain of the induced optical signal.

The device is not designed for radiation detection. Nevertheless, we find it useful to characterize the response to optical modulation by its noise equivalent power (NEP). Fig. 11 shows the NEP of the device for various optical modulation frequencies. Each NEP data point is derived out of several reflected power measurements in the vicinity of f_1 , where each measurement is performed with a different pump power, ranges between -54.7 dBm and -45.7 dBm . The best NEP is measured for a modulation frequency of $\Delta f = 10\text{MHz}$ and equals $38\text{fW}/\sqrt{\text{Hz}}$. A rather low NEP of $370\text{fW}/\sqrt{\text{Hz}}$ is measured for a modulation frequency of $\Delta f = 1.699\text{GHz}$. For this modulation frequency, f_1 coincides with the third resonance frequency of the resonator. Higher modulation frequencies than the ones presented in Fig. 11 are also observed, but the measured NEP is relatively poor, mainly due to the bandwidth limitations of the microwave components composing the experimental setup.

IV. DISCUSSION

Fast modulation of the resonance frequency is experimentally demonstrated. Furthermore, the parametric gain threshold condition is achieved in a CW measurement. The main problem, that currently prevents parametric gain to occur, is the relatively low photon flux that impinges the HED. Due to losses along the optical path, especially the expansion of the Gaussian beam from the tip of the fiber to the HED, the largest

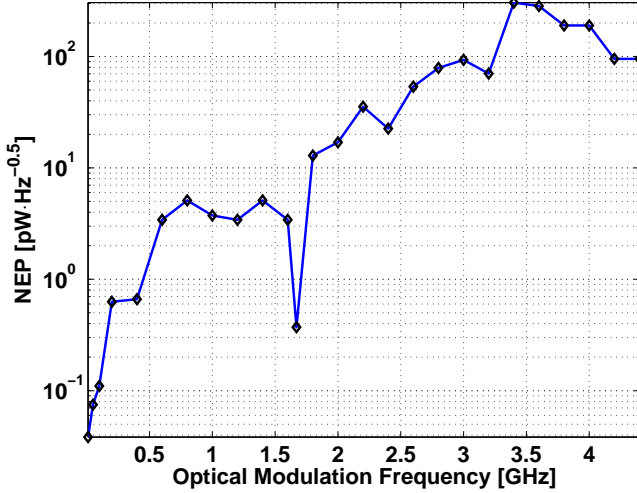


Fig. 11. NEP for various optical modulation frequencies.

photon flux we currently manage to apply is approximately 13 photons per modulation cycle, at twice the resonance frequency. Taking into account the effective area of the HED and its quantum efficiency [32] we estimate that the optical power flux is two orders of magnitude lower than the threshold power. Therefore parametric gain can not be achieved using the present device. Future devices will address this problem.

V. CONCLUSION

We have reviewed the design, fabrication, and measurement results of our optically tunable resonator. Resonance frequency modulation frequency as high as 4.2GHz is achieved, and a NEP of $38\text{fW}/\sqrt{\text{Hz}}$ in the IR is measured. The parametric gain threshold condition is achieved in a CW measurement. Moreover, the results are shown to be in a good agreement with a theoretical modeling. The approach used in this device has a great potential of achieving a parametric amplification in superconducting resonators.

APPENDIX DAMPING RARE EXTRACTION

The universal expression for the reflection amplitude of a linear resonator near resonance is [2], [33]

$$S_{11} = \frac{i\Omega + (\gamma_1 - \gamma_2)}{i\Omega - (\gamma_1 + \gamma_2)}, \quad (1)$$

where $\Omega = \omega_p - \omega_0$ is the pump angular frequency ω_p , relative to the angular resonance frequency ω_0 , γ_1 is the coupling constant between the resonator and the feedline, and γ_2 is the unloaded damping rate of the resonance. The damping rate is numerically extracted by expanding Eq. (1) to first order in Ω ,

$$S_{11} = r_0 + r_1\Omega + O(\Omega^2),$$

where r_0 is the S_{11} value at the resonance frequency,

$$r_0 = \frac{\gamma_2 - \gamma_1}{\gamma_1 + \gamma_2},$$

and r_1 is the slope of the imaginary part of S_{11} ,

$$r_1 = -i \frac{2\gamma_1}{(\gamma_1 + \gamma_2)^2}.$$

Note that the extraction of r_1 is less accurate for low Q -factor curves, and thus the calculated loss factor suffers from a rather large impreciseness at that regime.

REFERENCES

- [1] N. V. Fomin, O. L. Shalaevand, and D. V. Shantsev, "Parametric resonance in superconducting micron-scale waveguides," *J. Appl. Phys.*, vol. 81, no. 12, pp. 8091–8096, Jun. 1997.
- [2] B. Yurke and E. Buks, "Performance of cavity-parametric amplifiers, employing Kerr nonlinearities, in the presence of two-photon loss," *arXiv:quant-ph/0505018 v1*, pp. 1–9, 2005.
- [3] B. C. Sanders and G. J. Milburn, "Complementarity in a quantum nondemolition measurement," *Phys. Rev. A*, vol. 39, no. 2, pp. 694–702, Jan. 1989.
- [4] V. V. Dodonov and A. B. Klimov, "Generation and detection of photons in a cavity with a resonantly oscillating boundary," *Phys. Rev. A*, vol. 53, no. 4, pp. 2664–2682, Apr. 1996.
- [5] L. Landau and E. Lifshits, *Mechanics*. New York: Oxford, 1976.
- [6] M. A. Golosovsky, H. J. Snortland, and M. R. Beasley, "Nonlinear microwave properties of superconducting Nb microstrip resonators," *Phys. Rev. B*, vol. 51, no. 10, pp. 6462–6469, 1995.
- [7] G. N. Goltzman, A. Korneev, I. Rubtsova, I. Milostnaya, G. Chulkova, O. Minaeva, K. Smirnov, B. Voronov, W. Sysz, A. Pearlman, A. Verevkin, and R. Sobolewski, "Ultrafast superconducting single-photon detectors for near-infrared-wavelength quantum communications," *Phys. Status Solidi C*, vol. 2, no. 5, pp. 1480–1488, 2005.
- [8] S. Cho and C.-S. Son, "Modulation of the resonance frequency of superconducting microwave resonators," *IEEE Trans. Appl. Superconduct.*, vol. 13, no. 2, pp. 3659–3662, Jun. 2003.
- [9] —, "Observation of bolometric optical response in superconducting microwave meander lines," *J. Appl. Phys.*, vol. 84, no. 10, pp. 5657–5661, Nov. 1998.
- [10] M. Tsindlekht, M. Golosovsky, H. Chayet, and D. Davidov, "Frequency modulation of the superconducting parallel-plate microwave resonator by laser irradiation," *Appl. Phys. Lett.*, vol. 65, no. 22, pp. 2875–2877, Nov. 1994.
- [11] P. K. Day, H. G. LeDuc, B. A. Mazin, A. Vayonakis, and J. Zmuidzinas, "A broadband superconducting detector suitable for use in large arrays," *Nature*, vol. 425, pp. 817–821, Oct. 2003.
- [12] R. Wedenig, T. Niinikoski, P. Berglund, J. K. R. Inen, L. Costa, M. Valtonen, R. Linna, J. Salmi, H. SeppaK, and I. Suni, "Superconducting NbN microstrip detectors," *Nucl. Instrum. Methods Phys. Res. A*, vol. 443, no. 3, pp. 646–663, Sep. 1999.
- [13] K. Chang, S. Martin, F. Wang, and J. L. Klein, "On the study of microstrip ring and varactor-tuned ring circuits," *IEEE Trans. Microwave Theory Tech.*, vol. MTT-35, no. 12, pp. 1733–1739, Dec. 1987.
- [14] T. S. Martin, F. Wang, and K. Chang, "Theoretical and experimental investigation of novel varactor-tuned switchable microstrip ring resonator circuits," *IEEE Trans. Microwave Theory Tech.*, vol. 36, no. 12, pp. 1733–1739, Dec. 1988.
- [15] J.-C. Lee, H. F. Taylor, and K. Chang, "Degenerate parametric amplification in an optoelectronic GaAs CPW-to-slotline ring resonator," *IEEE Microwave Guided Wave Lett.*, vol. 7, no. 9, pp. 267–269, Sep. 1997.
- [16] G. K. Gopalakrishnan, B. W. Fairchild, C. L. Yeh, C.-S. Park, K. Chang, M. H. Weichold, and H. F. Taylor, "Experimental investigation of microwave-optoelectronic interactions in a microstrip ring resonator," *IEEE Trans. Microwave Theory Tech.*, vol. 39, no. 12, pp. 2052–2060, Dec. 1991.
- [17] D. Saeedkia, A. H. Majedi, S. Safavi-Naeini, and R. R. Mansour, "Frequency and time-varying scattering parameters of a photo-excited superconducting microbridge," *IEEE Microwave Wireless Compon. Lett.*, vol. 15, no. 8, pp. 510–512, Aug. 2005.
- [18] J. Zhang, W. Sysz, A. Verevkin, O. Okunev, G. Chulkova, A. Korneev, A. Lipatov, G. N. Goltzman, and R. Sobolewski, "Response time characterization of NbN superconducting single-photon detectors," *IEEE Trans. Appl. Superconduct.*, vol. 13, no. 2, pp. 180–183, Jun. 2003.
- [19] G. N. Goltzman, K. Smirnov, P. Kouminov, B. Voronov, N. Kaurova, V. Drakinsky, J. Zhang, A. Verevkin, and R. Sobolewski, "Fabrication of nanostructured superconducting single-photon detectors," *IEEE Trans. Appl. Superconduct.*, vol. 13, no. 2, pp. 192–195, Jun. 2003.

- [20] B. Abdo, E. Segev, O. Shtempluck, and E. Buks, "Observation of bifurcations and hysteresis in nonlinear NbN superconducting microwave resonators," *cond-mat/0501114* v2, 2005.
- [21] B. Delaeta, J.-C. Villegierb, W. Escoffierb, J.-L. Thomassinb, P. Feautriera, I. Wangc, P. Renaud-Goudc, and J.-P. Poizat, "Fabrication and characterization of ultra-thin NbN hot electron bolometer for near infrared single photon detection," *Nucl. Instr. and Meth. A*, vol. 520, pp. 541–543, 2004.
- [22] A. Lichtenberger, D. Lea, and F. Lloyd, "Investigation of etching techniques for superconducting Nb/Al-Al₂O₃/Nb fabrication processes," *IEEE Trans. Appl. Superconduct.*, vol. 3, no. 1, pp. 2191–2196, Mar. 1993.
- [23] A. V. Gurevich and R. G. Mints, "Self-heating in normal metals and superconductors," *Rev. Mod. Phys.*, vol. 59, no. 4, pp. 941–999, Oct. 1987.
- [24] J. Zhang, W. Slysz, A. Pearlman, A. Verevkin, R. Sobolewski, O. Okunev, G. Chulkova, and G. N. Goltsman, "Time delay of resistive-state formation in superconducting stripes excited by single optical photons," *Phys. Rev. B*, vol. 67, 132508, 2003.
- [25] B. Abdo, E. Segev, O. Shtempluck, and E. Buks, "Nonlinear dynamics in the resonance lineshape of NbN superconducting resonators," *cond-mat/0601146*, 2006.
- [26] P. Gardner, D. K. Paul, and K. P. Tan, "Planar microstrip ring resonator filters," *Antennas for Personal Communication Systems, IEE Colloquium*, pp. 6/1 – 6/6, Feb. 1994.
- [27] S. M. Anlage, H. J. Snortland, and M. R. Beasley, "A current controlled variable delay superconducting transmission line," *IEEE Trans. Magn.*, vol. 25, no. 2, pp. 1388–1391, Mar. 1989.
- [28] S. Cho, J.-C. Park, and C. Lee, "Current and temperature controlled variable inductance insuperconducting microstrip lines," *IEEE Trans. Appl. Superconduct.*, vol. 11, no. 1, pp. 3090–3093, Mar. 2001.
- [29] R. E. Collin, *Foundations for Microwave Engineering*, 2nd ed. New York: McGraw-Hill, 1992, pp. 538–541.
- [30] B. Abdo, E. Segev, O. Shtempluck, and E. Buks, "Intermodulation gain in nonlinear NbN superconducting microwave resonators," *Appl. Phys. Lett.*, vol. 88, no. 1, Jan. 2006, to be published.
- [31] E. Segev, B. Abdo, O. Shtempluck, and E. Buks, *In preparation*.
- [32] A. Korneev, P. Kouminov, V. Matvienko, G. Chulkova, K. Smirnov, B. Voronov, G. N. Goltsman, M. Currie, W. Lo, K. Wilsher, J. Zhang, W. Slysz, A. Pearlman, A. Verevkin, and R. Sobolewski, "Sensitivity and gigahertz counting performance of NbN superconducting single-photon detectors," *Appl. Phys. Lett.*, vol. 84, no. 26, pp. 5338–5340, Jun. 2004.
- [33] B. Abdo, E. Segev, O. Shtempluck, and E. Buks, "Nonlinear coupling in Nb/NbN superconducting microwave resonators," Jan 2005, arXiv:cond-mat/0501236 v1.

Oleg Shtempluck was born in Moldova in 1949. He received the M.Sc. degree in electronic engineering from the physical department of Chernovtsy State University, Soviet Union, in 1978. His research concerned semiconductors and dielectrics. From 1983 to 1992, he was a team leader in the division of design engineering in Electronmash factory, and from 1992 to 1999 he worked as stamp and mould design engineer in Ikar company, both in Ukraine. Currently he is working as a laboratory engineer in Microelectronics Research Center, Technion- Israel Institute of Technology, Haifa, Israel.

Eyal Buks received the B.Sc. degree in mathematics and physics from the Tel-Aviv University, Tel-Aviv, Israel, in 1991 and the M.Sc. and Ph.D. degrees in physics from the Weizmann Institute of Science, Israel, in 1994 and 1998, respectively. His graduate work concentrated on interference and dephasing in mesoscopic systems. From 1998 to 2002, he worked at the California Institute of Technology (Caltech), Pasadena, as a Postdoctoral Scholar studying experimentally nanomachining devices. He is currently a Senior Lecturer at the Technion—Israel Institute of Technology, Haifa. His current research is focused on nanomachining and mesoscopic physics.

Eran Segev-Arbel was born in Haifa, Israel in 1975. He received the B.Sc. degree in electrical engineering from the Technion—Israel Institute of Technology, Haifa, Israel, in 2003. He is currently working toward the M.Sc. in electrical engineering at the Technion. His research is focused on parametric gain in superconducting microwave resonators.

Baleegh Abdo (S'2002) was born in Haifa, Israel in 1979. He received the B.Sc. degree in computer engineering, in 2002, and the M.Sc. degree in electrical engineering in 2004, both from the Technion—Israel Institute of Technology, Haifa, Israel. Currently he is pursuing the Ph.D. degree in electrical engineering at the Technion. His graduate research interests are nonlinear effects in superconducting resonators in the microwave regime, resonator coupling and quantum computation.